Bioactive Materials 45 (2025) 584–598

Contents lists available at ScienceDirect

Bioactive Materials

journal homepage: www.keaipublishing.com/en/journals/bioactive-materials

Mechanically robust surface-degradable implant from fiber silk composites demonstrates regenerative potential

Wenhan Tian [a], Yuzeng Liu [b,**], Bo Han [b], Fengqi Cheng [b], Kang Yang [d], Weiyuan Hu [a], Dongdong Ye [e], Sujun Wu [a], Jiping Yang [a], Qi Chen [f], Yong Hai [b], Robert O. Ritchie [c,***], Guanping He [b,****], Juan Guan [a,g,*]

[a] School of Materials Science and Engineering, Beihang University, Beijing, 100191, PR China
[b] Department of Orthopedics, Capital Medical University Affiliated Beijing Chaoyang Hospital, Capital Medical University, Beijing, 100020, PR China
[c] Department of Materials Science & Engineering, University of California, Berkeley, CA, 94720, USA
[d] School of Materials Science and Engineering, Anhui University of Technology, Maanshan, Anhui, 243002, PR China
[e] College of Light Textile Engineering and Art, Anhui Agricultural University, Hefei, Anhui, 230036, PR China
[f] Ningbo Regen Biotech Co., Ltd., Ningbo, Zhejiang, 315157, PR China
[g] Beijing Advanced Innovation Center for Biomedical Engineering, Beijing, 100083, PR China

ARTICLE INFO

Keywords:
Hierarchical structure
Continuous fiber silk
Regenerative biomaterial
Cell-mediated degradation
Macrophage polarization

ABSTRACT

Through millions of years of evolution, bones have developed a complex and elegant hierarchical structure, utilizing tropocollagen and hydroxyapatite to attain an intricate balance between modulus, strength, and toughness. In this study, continuous fiber silk composites (CFSCs) of large size are prepared to mimic the hierarchical structure of natural bones, through the inheritance of the hierarchical structure of fiber silk and the integration with a polyester matrix. Due to the robust interface between the matrix and fiber silk, CFSCs show maintained stable long-term mechanical performance under wet conditions. During *in vivo* degradation, this material primarily undergoes host cell-mediated surface degradation, rather than bulk hydrolysis. We demonstrate significant capabilities of CFSCs in promoting vascularization and macrophage differentiation toward repair. A bone defect model further indicates the potential of CFSC for bone graft applications. Our belief is that the material family of CFSCs may promise a novel biomaterial strategy for yet to be achieved excellent regenerative implants.

1. Introduction

Presently, bone damage induced by aging, trauma, and diseases exhibits a persistent increase globally. Despite significant efforts towards bone substitutions, many patients still face challenges such as stress shielding, osteoporosis caused by high modulus implants, secondary surgeries, and chronic inflammation due to non-degradable implants [1,2]. Despite of decades of effort in the medics, researchers are still seeking ideal artificial bone implants to address these clinical issues [3,4]. The materials for ideal implants should simultaneously satisfy the following requirements: i) possess comprehensive mechanical properties (modulus and strength) equivalent to or superior to the bone tissues; ii) be stably absorbable or degradable; iii) promote osteogenesis [1,5].

Natural bones exhibit an elastic modulus of 0.2–20 GPa and an ultimate strength of approximately 150 MPa owing to the delicate hierarchical morphology composed of collagen fibers and hydroxyapatite crystals [6–8]. Currently, biodegradable polymers such as polylactic acid (PLA) [9], polycaprolactone (PCL) [10], poly(lactic-co-glycolic acid) (PLGA) [11] and polyurethane (PU) [12] have been extensively investigated for potential orthopedic degradable implants. These polyesters possess highly customizable chemical structures and crystalline morphologies as well as a wide-spectrum of mechanical and degradation properties. Among polyesters, PCL exhibits remarkable extensibility and toughness, and mainly undergoes slow surface degradation through

* Corresponding author. School of Materials Science and Engineering, Beihang University, Beijing, 100191, PR China.
** Corresponding author.
*** Corresponding author.
**** Corresponding author.
E-mail addresses: beijingspine2010@163.com (Y. Liu), roritchie@lbl.gov (R.O. Ritchie), bjspine_hgp@sina.com (G. He), juan.guan@buaa.edu.cn (J. Guan).

https://doi.org/10.1016/j.bioactmat.2024.11.036
Received 2 July 2024; Received in revised form 12 November 2024; Accepted 28 November 2024

hydrolysis and lipid enzyme-catalysis *in vivo* [13]. Such behaviors mitigate the risk of catastrophic failure and compulsory secondary surgeries after implantation [14]. However, the low elastic modulus, low strength, surface hydrophobicity, and excessively slow degradation rate of PCL limit its application scope and repair efficacy in the field of orthopedics. To address these issues, nano-reinforcements such as barium-doped calcium silicate particles were employed to enhanced the mechanical properties of bulk or scaffold PCL [15]. The biocompatible particles can also enhance the material's biological performance [5,16,17]. Nevertheless, previous research has rarely reported on achieving a strength exceeding 120 MPa to suffice for bone implant applications [18]. To tune the degradability of PCL, additives were commonly introduced to modify the crystalline morphology, thus to regulate their progressive depolymerization/hydrolisis behavior [19]. Notably, some polyesters were shown to exhibit an interesting cell-mediated dissolution mechanism controlled by host cells [13,20–22].

Composed of amino acids, silk is the only protein fiber with macroscopic continuity (beyond 1 km) and a highly ordered multi-scale structure [23–25]. These unique properties not only provide excellent processability as a textile material and biocompatibility for biomedical applications, but also endow it with comprehensive mechanical properties that may be suitable for bone implant applications [25–29]. Over many centuries, natural silk has been utilized for the manufacturing of textiles and clinical sutures [30,31]. Currently, the advancements in "silk biomaterials" largely focus on the extracted silk fibroin and sericin, with the goal of generating innovative materials in various fields, including energy, drug delivery, catalysis, and regenerative medicine [23,32–37]. The prevailing methodology to extract silk fibroin entails the use of solvents to disrupt the hydrogen bond network in the crystalline region of natural silk [18,38]. However, the natural silk's elegant macroscopic continuity and multiscale structure are inevitably damaged during the processing. The result is a largely different structure-property relationship for regenerated silk materials [39].

In this work, we adore the hierarchical structure and comprehensive performance of natural fiber silks and persist to use natural fiber silk for structural biomaterials. A new family of biomaterials, namely continuous fiber silk composites (CFSCs), are designed based on continuous fiber silk in the form of yarns and fabrics, and degradable polyester for use as degradable implants *in vivo*. By inheriting the hierarchical structure of fiber silk, we aim to achieve a balance between strength, modulus and degradability for CFSCs. By conducting *in vitro* and *in vivo* degradation experiments for 6 months, we will evaluate the long-term mechanical stability of CFSCs and reflect on the degradation mechanism. In particular, the material-macrophage interactions will be investigated, which regulate the degradation *in vivo*. Our study will provide comprehensive assessments on the new family of silk biomaterials for use in potential degradable implants for regenerative medicine.

2. Results and discussion

2.1. Design and fabrication of bone-mimetic multi-scale structures of fiber silk composites

The pursuit of ideal degradable medical implants has consistently focused on achieving a balance of matched modulus, high strength, high toughness and degradation rate to avoid premature wear and failure prior to the full regeneration (Fig. 1a). Natural bones achieve these balanced mechanical properties through manipulating compositions and structures across multiple scales. Traditional biodegradable implant materials such as bulk PCL, lacking these complex multiscale structures, have always failed to elevate strength to levels similar to load-bearing bones. Herein, we fabricated macro-scale composites CFSCs using continuous fiber silk as the reinforcing phase and thermoplastic polyester as the matrix. Fig. 1b shows, a series of CFSCs were successfully fabricated by applying hot-pressing and layer-by-layer assembly techniques. Subsequent mechanical processing can yield various forms such as sheets, tubes, and others. The silk content in the composite can be conveniently controlled by the fabric numbers and mold sizes. CFSCs with different fiber volume fractions, denoted as 20 % fiber silk CFSCs, 40 % fiber silk CFSCs, and 60 % fiber silk CFSCs groups (or simply 20%/40%/60%-CFSCs) were prepared. In the schematics of Fig. 1c, we compare the multi-scale hierarchical structure of CFSC and bone. The CFSC contains laminates at the sub-macro scale, which further consist of microscale fiber silks and a matrix. The fiber silk can be seen as β-sheet crystal-reinforced fibroin composite at the nanoscale. Thus, the CFSCs with such a structural hierarchy and heterogeneous compositions may emulate the mechanical performance of natural bones.

As protein-based natural fibers, fiber silks are sensitive to moisture and heat, exhibiting notable variability in mechanical performance [40,41]. We evaluated the average mechanical performance of single fibers for the effect of thermal treatments, and employed the Weibull distribution analysis for measure of reliability throughout their service [42–45].The results in Figs. S1–S5 indicate that fiber silk can endure exposure to temperatures as high as 170 °C without compromising their overall tensile properties, which allows for the processing of many degradable polyesters such as PCL, PLA, and PLGA. Our previous research showed that 120 °C should be the optimal melt-processing temperature for the silk-PCL composite filament [46]. We chose the same temperature for processing PCL with a suitable viscosity to fabricate CFSCs.

2.2. Tailorable properties of CFSCs

Fiber silk, due to their unique multi-scale structure, exhibits greater modulus and strength that surpass many bulk synthetic materials. With 40 % silk content, PLA-CFSCs exhibited a six-fold fracture toughness than the rigid and brittle bulk PLA; and PCL-CFSCs increased the tensile strength of soft and tough PCL by a factor of five (Fig. 2a and b). This demonstrates the significant effect of our silk reinforcement strategy.

The modulus and strength of a composite commonly increase with the reinforcement fiber content. When the fiber silk content increased from 20 % to 40 %, the modulus increased from 0.61 GPa to 1.05 GPa, and the compressive strength of CFSCs rose from 71 MPa to 160 MPa (Fig. 2c). However, further increase in the fiber silk content to 60 % did not result in a significant improvement in modulus and strength. Such combinations of modulus and strength especially the strength for CFSCs make it quite unique in the comparison diagram with bulk polymers such as PLA and PEEK (Fig. 2d). It is noted that the modulus of CFSCs is closer to that of vertebrae cancellous bone (0.4 GPa). As observed in Fig. 2e, the interfacial shear strength of the 60%-CFSCs group decreased, which can be attributed to the insufficient encapsulation of the fibers by PCL. Additionally, scanning electron microscopy (SEM) images of 60%-CFSCs showed extensive exposure of fiber silk on the material surface (Fig. 3d), rendering the reinforcement less effective. Therefore, for the optimal reinforcement effect, CFSCs should possess fiber silk content below 60 %.

Compared to PCL, CFSCs also exhibit a significantly lower surface contact angle (Fig. 2f). It may be ascribed to the synergistic effect of the high water-absorbing property of the fiber silk (20-30 wt%) and the capillary phenomenon at the fiber-matrix interface.

CFSCs also exhibit remarkable thermoforming capabilities and processability. Fig. 2g shows the microstructure of CFSCs with 20 % or 40 % fiber silk. The silk yarns appear compact and well-integrated with the PCL matrix. When heated above the glass transition temperature (T_g) of the matrix polymer, it will deform and re-mold easily, facilitating the intricate design of helical slices, tubular structures, and lattice structures based on CFSCs (Fig. 2h). Furthermore, compact bulk CFSCs are stiff enough to be machine-processed into rod shapes, cages, and bone nails.

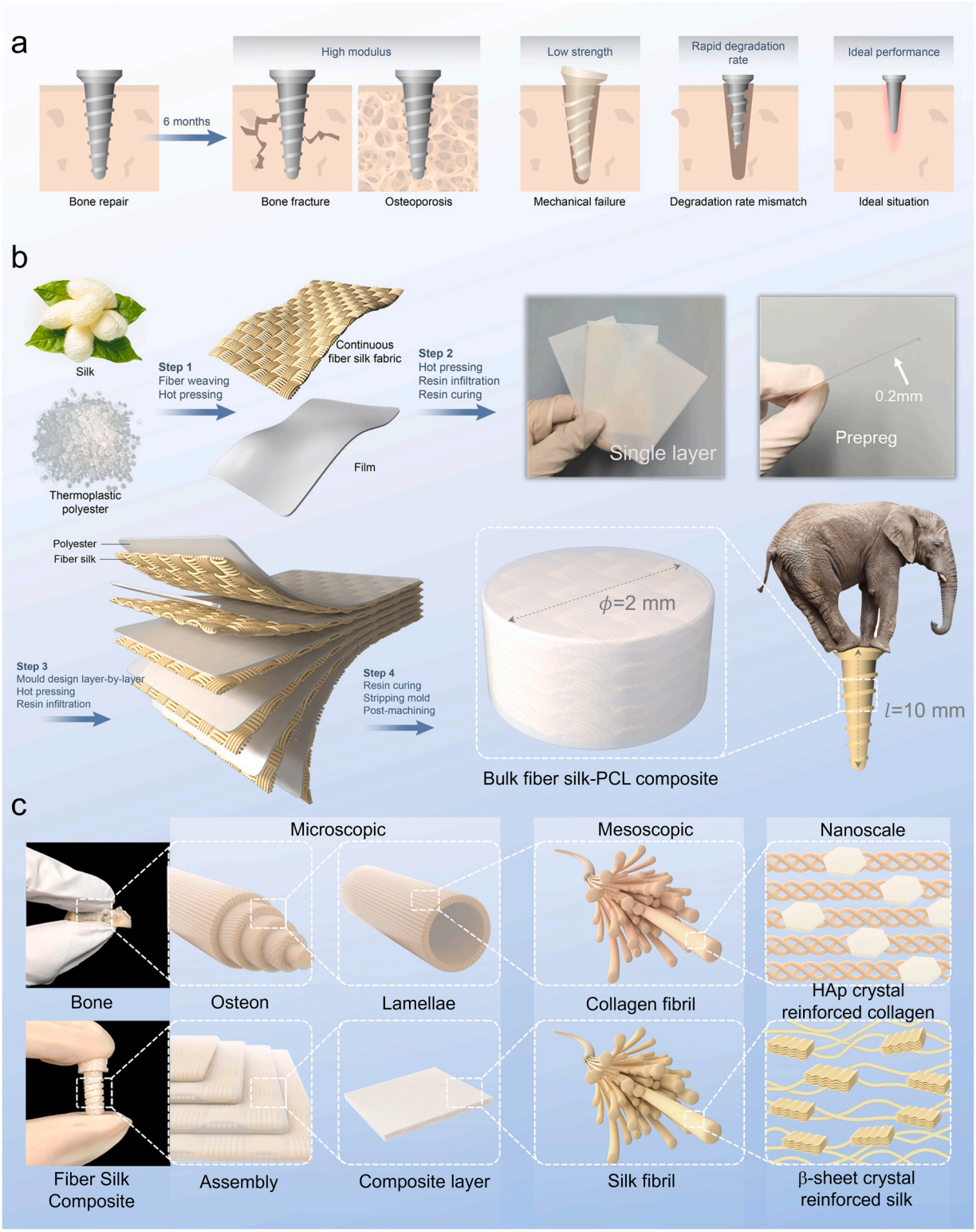

Fig. 1. Illustration of the preparation process of the CFSCs. (**a**), Different bone repair and regeneration effects induced by incompatible properties of bone graft materials. (**b**), Utilizing a physical processing approach or thermal and pressure molding, natural continuous fiber silks are prepared into three-dimensional silk-based materials that retain macroscopic continuity and the multi-level structure of continuous fiber silk. Step 1: Preparation of silk fabric and the thermoplastic polyester film. Step 2: Hot-pressing or pressure-driven melt fusion to produce single layer prepregs. Step 3: Prepregs are assembled layer-by-layer, and bulk CFSCs are prepared by a 2nd hot-pressing. Step 4: Post-machining to achieve desired shapes. (**c**), Illustrations of the multi-scale hierarchical structure of CFSC and natural bone. In CFSC, continuous fiber silk in the composite lamella is further composed of micro-/nanofibers with a semicrystalline morphology; in bone, the bone lamella is composed of collagen fibrils with tropocollagen nanorods and hydroxyapatite nanocrystals. Such unique hierarchical structure forms the basis for their surprising performance.

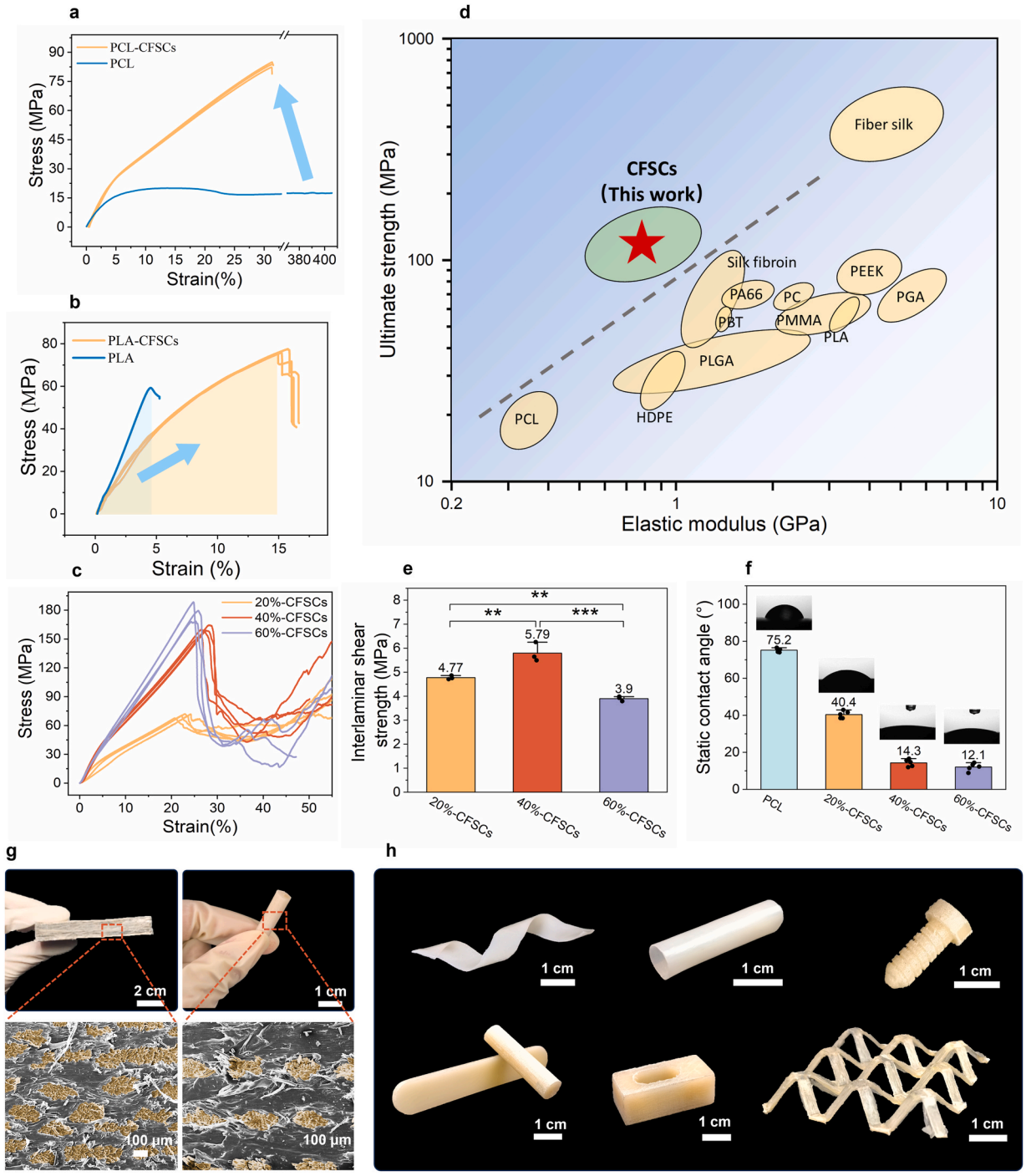

Fig. 2. Comprehensive assessments of CFSCs. (**a**) Tensile stress-strain curves of soft and tough PCL and PCL-CFSCs. Fiber silk can increase the strength of materials (n = 3). (**b**) Tensile stress-strain curves of hard and brittle PLA and PLA-CFSCs. Fiber silk can increase material toughness (n = 3). (**c**) Compression stress-strain curves of 20%, 40% and 60%-CFSCs groups using PCL as the matrix (the same for the rest of the figures) (n = 4). (**d**) Comparison of mechanical properties of CFSCs, fiber silk and other mainstream polymer materials. (**e**) ILSS of 20%, 40% and 60%-CFSCs groups (n = 3). (**f**) Static contact angle of water on PCL, 20%, 40% and 60%-CFSCs groups (n = 5). (**g**) Macro photos of CFSCs and SEM images of the microstructure with fiber silk volume fractions of 20 % and 40 %, respectively. (**h**) Photographs of CFSCs, including a spiral thin slice, rod, thin-walled tube, cage, bone nail, and lattice structure, fabricated by thermal processing, pressing-driven fusion and post-machining. One-way analysis of variance (ANOVA) was used to determine statistical differences between the groups. The statistical significance was designated as * for $p < 0.05$, ** for $0.01 < p < 0.05$, and *** for $0.001 < p < 0.01$.

2.3. Hydration and in vitro degradation of CFSCs

The principal degradation mechanisms of biodegradable materials *in vivo* include corrosion, hydrolysis, and cell-mediated absorption. Currently, mainstream degradable materials exhibit mostly random corrosion and bulk hydrolysis. Here, we conducted a 180-day *in vitro* degradation experiment on CFSCs immersed in 37 °C phosphate buffered saline (PBS) to elucidate on their degradation mechanisms (Fig. 3a).

After 60 days of static immersion, CFSCs reached saturation water contents of approximately 4 %, 10 %, and 17 %, respectively corresponding to 20 %, 40 % and 60 % fiber silk contents (Fig. 3b). Dry mass

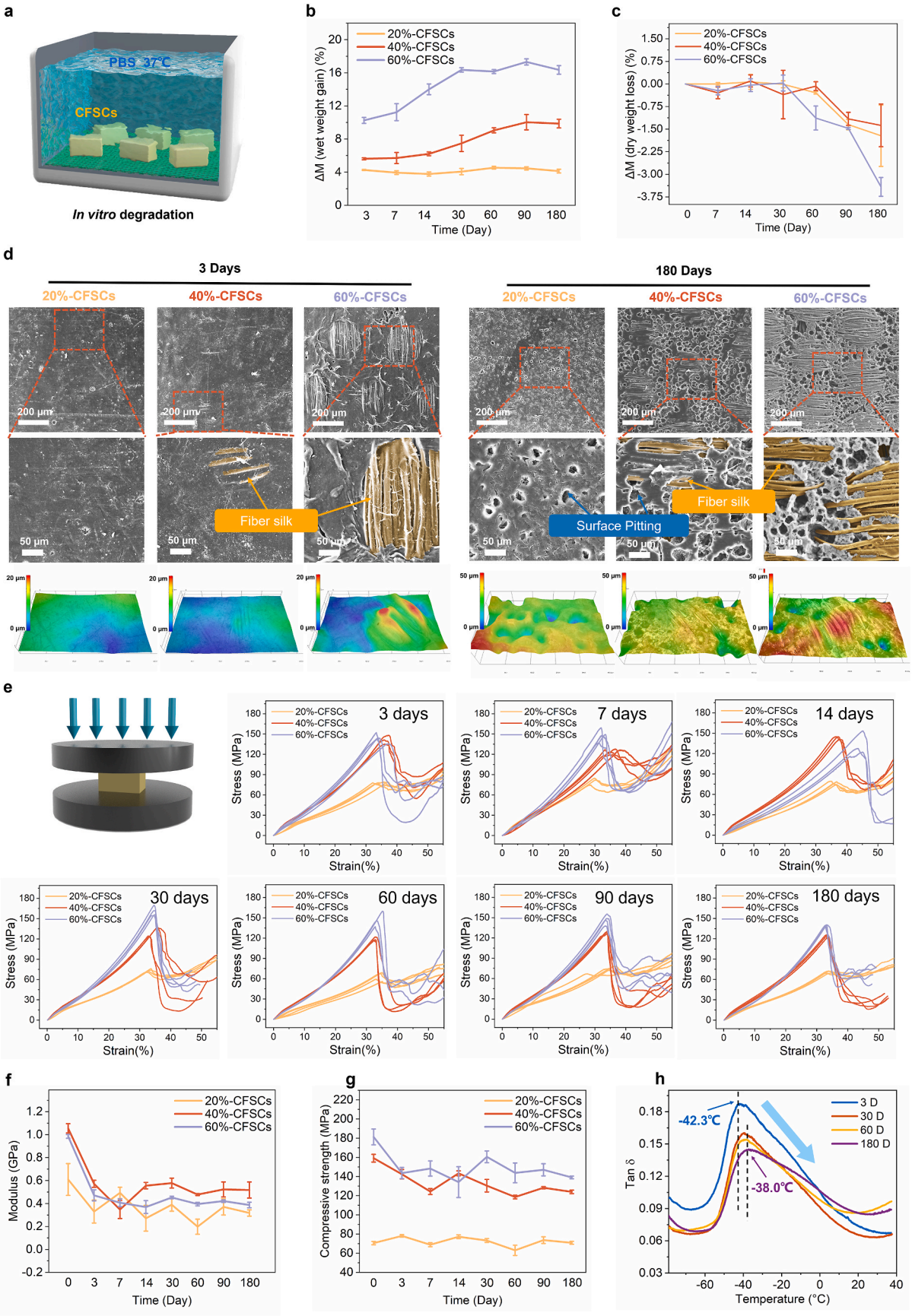

(caption on next page)

Fig. 3. The mechanical stability of CFSCs in the 180-days *in vitro* degradation. (**a**) Illustration of the *in vitro* degradation experiment. (**b and c**), Wet weight (b) and dry weight (c) of 20%-CFSCs, 40%-CFSCs and 60%-CFSCs groups at different times of degradation (n = 4). (**d**) Upper surface morphology from SEM and SDF of 20%-CFSCs, 40%-CFSCs and 60%-CFSCs groups after 3 or 180-days of degradation (**e**) Compressive stress-strain curves of the CFSCs after 3 days, 7 days, 14 days, 30 days, 60 days, 90 days, and 180-days of degradation (n = 4). (**f and g**) Compressive modulus (f) and compressive strength (g) of 20%-CFSCs, 40%-CFSCs and 60%-CFSCs groups at different times of degradation (0-day samples were dry, and the rest samples were wet) (n = 4). (**h**) Dynamic mechanical analysis (DMA) measured loss tangent *tanδ* - temperature curves from −80 °C to 40 °C from dynamic mechanical thermal analysis on the dried 40%-CFSCs group after 3 days, 30 days, 60 days and 180-days of degradation.

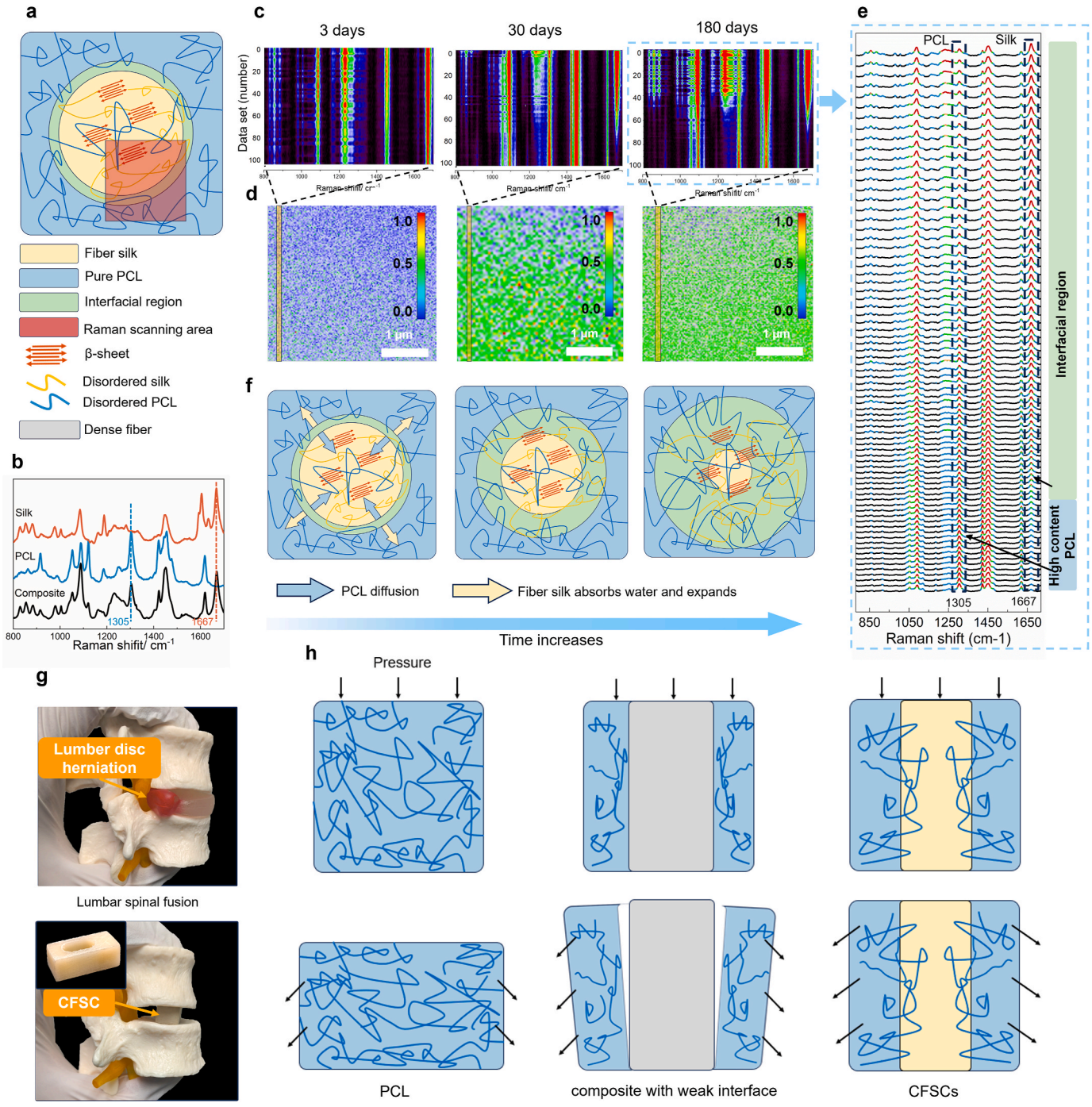

Fig. 4. Interface changes of CFSCs in the 180-days *in vitro* degradation. (**a**) Illustrations of the scanning region of Raman measurements. (**b**) Characteristic Raman spectra of fiber silk, pure PCL and 40%-CFSCs. (**c, d**), 2D pseudo-colored representations from Raman line scans (c) and Raman area scans (d) across the composite interface regions of the dry 40%-CFSCs group after 3 days, 30 days and 180-days of degradation. (**e**) Raman spectra with pseudo-colored peaks from one line-scan across the interface regions of the 40%-CFSCs group after 180-days of degradation. (**f**) Illustrations of the interface compositional changes driven by osmotic pressure of water and molecular motions of PCL during the PBS submersion degradation. (**g**) Lumber disc herniation and Cage (CFSCs) models. (**h**) Illustrations on the probable failure modes and toughening mechanism of pure PCL, composite with weak interface, and CFSCs, after stress application.

of CFSCs continued to decrease by 1.72 %, 1.38 %, and 3.42 % at 180 days, respectively for 20%, 40%, and 60%-CFSCs (Fig. 3c). It indicated the hydrolysis of PCL took place very slowly in PBS over 180 days.

SEM images and super depth-of-field microscopy (SDF) 3D images (Fig. 3d) showed evident surface pitting in 60%-CFSCs, yet no significant internal changes were observed inside the material (Fig. S6). It indicated a surface degradation mechanism for CFSCs in PBS.

We further evaluated the change in the mechanical properties of CFSCs during *in vitro* degradation. Fig. 3e shows the compressive stress-strain curves for wet 20%-CFSCs, 40%-CFSCs, and 60%-CFSCs specimens at different degradation times. During the initial three days, the transition of the material from a dry to wet state resulted in a substantial reduction in the compressive modulus of 20%, 40%, and 60%-CFSCs to 0.36, 0.65, and 0.41 GPa (Fig. 3f). Compressive strengths also fast decreased to 78, 142, and 143 MPa, respectively (Fig. 3g). For the wet composites, the reduction in the strength and modulus were approximately proportional to the silk content. Although the modulus of wet 60%-CFSCs was lower than that of 40%-CFSCs, the strengths of both groups remained similar. After the initial hydration until 180 days, no significant decrease was observed in the compressive strength and modulus across all groups.

The fiber-matrix interfaces in fiber reinforced composites could be the most susceptible to damage especially in the aging processes [47–49]. Our compressive test of CFSCs indicated that interfacial delamination was one critical failure mode (Fig. S11). Therefore, we further study the changes at the interface on molecular levels using Dynamic Mechanical Analysis (DMA), X-ray diffraction, and Raman Imaging Analysis. The *tan*δ profile in Fig. 3h from DMA reveals a reduced peak height and elevated peak temperature, indicating a suppressed glass transition of the PCL phase in 40%-CFSCs. This may imply an increased crystallinity in the residual PCL or intensified interactions between PCL and silk that restrict the segmental motions of PCL. However, X-ray diffraction (XRD) analysis suggested negligible variations in PCL crystal structure and crystallinity (Fig. S12). Therefore, we deduce that the suppressed molecular motions in the amorphous PCL after degradation could be due to the enhanced interactions with silk at the interface. This further suggested robust interfaces of the composite that can resist degradation.

To discern molecular changes at the silk-PCL interface, Raman spectroscopy (Fig. 4a) on the internal structure of the 40%-CFSCs [46]. Fig. 4b denotes peaks at 1667 cm^{-1} for the fiber silk (Amide I band) and the peak at 1305 cm^{-1} for the PCL. The spectrum without new peaks confirms that fiber silk and PCL formed a physically fused interface without covalent interactions. Interestingly, 'thermal' maps (Fig. 4c) from the line scans indicated that PCL could gradually diffuse into the body of fiber silk over time. In the surface scan mode, we computed the ratio of the peak intensity at 1305 cm^{-1} to that at 1667 cm^{-1} for each Raman spectrum, assigning (false) colors to single pixels based on the calculated ratio. Subsequently, tens of thousands of Raman spectra were analyzed to portray the relative content of PCL across the entire interface (Fig. 4d and e, Fig. S14). As the degradation progresses, large blue regions of dominant fiber silk transition to other colored regions of the interwoven fiber silk-PCL interface. As depicted in the schematic in Fig. 4f, PCL gradually diffused toward the interior of the fiber silks, which were soaked in water and swollen. These analyses proved that during *in vitro* degradation the interfaces in CFSCs did not deteriorate, but somehow were enhanced.

We fabricated a spinal fusion cage (Cage) model from CFSCs to demonstrate its mechanical robustness (Fig. 4g). Cage as a spinal implant device for surgical treatment of lumber disc herniation, represents a mechanically demanding implant. Pure PCL and other fiber reinforced composites were also proposed for fusional cages. As Fig. 4h shows, under complex stresses, PCL cage would deform largely due to insufficient stiffness; weakly bonded fiber-matrix composites would fail at the interface. CFSCs with robust interfaces would retain robust structural integrity to resist wet mechano-deterioration.

2.4. In vitro cyto-compatibility assessments

We evaluated the cell-material interplay by the co-culturing of CFSCs and MC3T3-E1 cells (Mouse osteoblast cell line) and conducting CCK-8 test, live/dead staining and cytoskeleton fluorescence measurement. 40%-CFSCs exhibited the highest cell density with the best-spread cell morphology (Fig. S15). On the 5th day of incubation, the cells on the CFSCs surface showed a higher density of nucleus and more elongated cytoskeletons compared to the PCL group (Fig. 5a). Cells were found to entangle around the filamentous fiber silk and even actively send out tentacles to wrap the fiber silk (Fig. 5b).

Quantitative analysis revealed a slight decrease in cell viability in the 20%-CFSCs and 40%-CFSCs groups on the first day, which may be attributed to the material transitioning from a dry to a wet state. However, from Day 3 to Day 5, cell viability in the 20%-CFSCs and 40%-CFSCs groups significantly surpassed that of the PCL group (Fig. 5c). Live/dead staining images in Fig. S16 proved that the CFSCs groups at Day 5 showed greater numbers of live cells and less dead cells. Further fluorescence quantitative analysis of the cytoskeletons showed that 40%-CFSCs had optimal spread and relaxed morphology (Fig. 5d and e). These results suggest that fiber silk could significantly enhance cell proliferation *in vitro*.

2.5. Animal model-based in vivo assessments

2.5.1. Cell-mediated degradation in vivo

Although CFSCs exhibited bulk hydrolysis resistance *in vitro*, degradation *in vivo* is believed to exert more complex mechanical and biological stresses on the implant. Subcutaneous implantation of 20%-CFSCs, 40%-CFSCs, fiber silk, and PCL groups was performed in a rat model, with observations made at 30, 90, and 180 days to assess *in vivo* degradation behavior. The general views on the whole implant and the material-tissue interface are shown in Fig. S17.

Throughout the entire degradation period, the border between PCL and tissue consistently maintained clarity, showing no evident signs of degradation (Fig. 6a). Although PCL induced a significant inflammatory response in the first month, its inherent hydrophobicity and non-affinity of cells led to material encapsulation by tissue, and resulted in a marked reduction in inflammatory cells after three months, agreeing with the literature [50]. Conversely, pure fiber silk, due to water-absorption property, cell-affinity and low immunogenicity, elicit only a mild inflammatory response with small numbers of inflammatory cells around the material (Fig. S18). Notably, silks can be stained a distinctive pink color by the Masson dye.

The CFSCs in the 20%-CFSCs and 40%-CFSCs groups showed significantly altered degradation behavior with the composite morphology. A substantial amount of PCL initially induced a pronounced inflammatory response. In the meanwhile, the fiber silk significantly enhanced the overall cellular activity and prevented the fibrous capsule from completely isolating the material from the tissue. As a result, there was a sustained expression of inflammatory cells around the CFSCs (Fig. 6a). As shown in Fig. S17, at 30 days, a thin layer of new tissue began forming around the material. At 90 days, there was a distinct inward displacement of the material-tissue interface in 20%-CFSCs. At 180 days, a substantial portion of the material had been replaced by tissue.

Masson's analysis in Figs. S19 and S20 showed as the PCL matrix was gradually metabolized by the host, the pink-colored fiber silks also diminished in size; some even disappearing (Fig. S21). Based on the spatial distribution of pink fiber silk and undegraded regions, Masson's images were artificially re-colorized (Fig. 6b and c). Semi-quantitative analysis revealed that after 180 days *in vivo*, the 20% and 40%-CFSCs had been respectively metabolized by approximately 81 % and 45 % (Fig. 6d). This difference in degradation rate is interesting. It may be attributed to the relatively lower fiber silk content in 20%-CFSCs and fiber silks are more stable than the PCL component. Additionally, due to

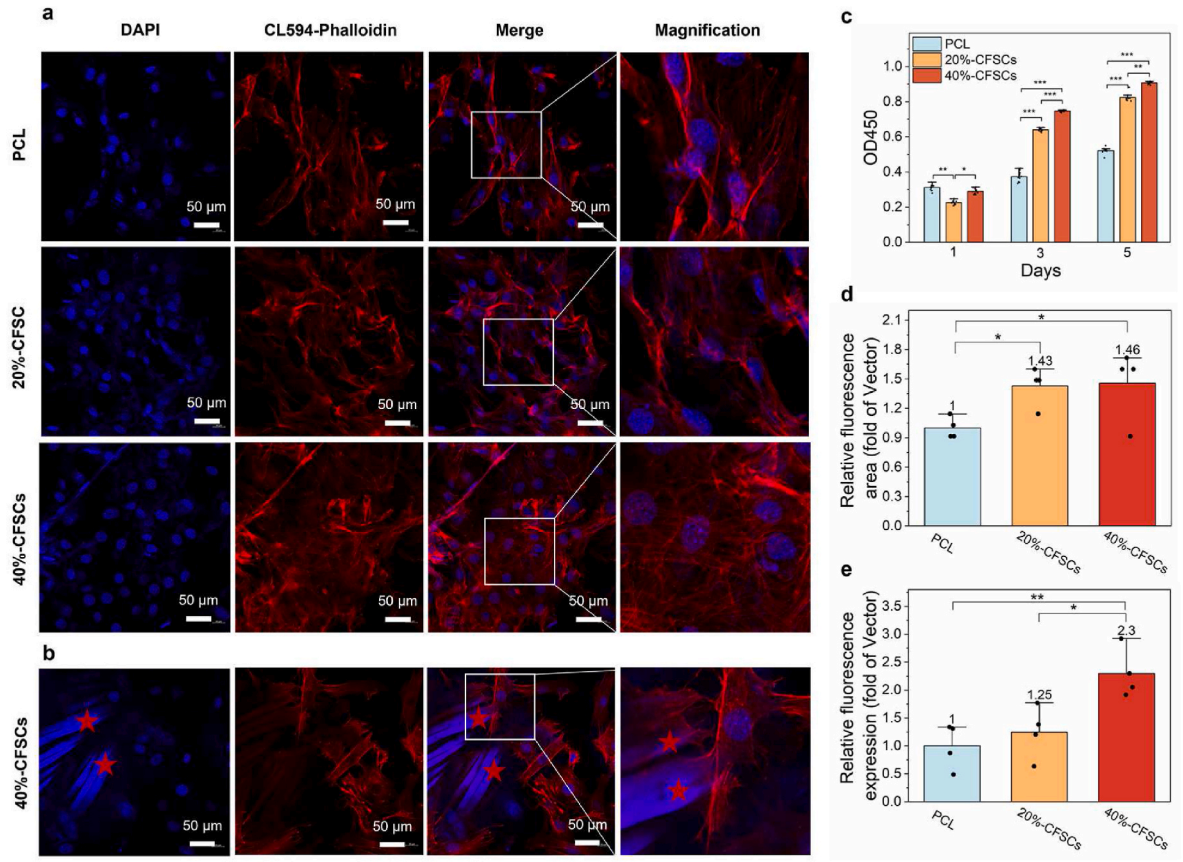

Fig. 5. *In vitro* cyto-compatibility assessments. (**a, b**) Fluorescence images of DAPI and Phalloidin stained MC3T3-E1 cells from co-culture of cells and materials of PCL, 20%-CFSCs, and 40%-CFSCs. DAPI and Phalloidin dyes stain the nucleus and the fiber F-actin constituted cell skeleton respectively. Red stars in (b) denote fiber silk bound with blue DAPI dye, highlighting the cellular affinity of fiber silk. (**c**), Optical density (OD) values of three cell groups from CCK-8 kits after co-culture of cells and three materials (n = 10). (**d, e**) Quantitative relative fluorescence area (d) and relative fluorescence expression (e) of the fluorescent images of various groups of MC3T3-E1 cells stained with Phalloidin on Day 5 (n = 4). One-way analysis of variance (ANOVA) was used to determine statistical differences between the groups. The statistical significance was designated as * for $p < 0.05$, ** for $0.01 < p < 0.05$, and *** for $0.001 < p < 0.01$.

such a fast degradation, the 20%-CFSCs induced excessive inflammatory response later after 3 months and unorganized necrotic lesions (Fig. S22).

Compared with the *in vitro* degradation, the *in vivo* degradation of 40%-CFSCs was over 40 times higher in the mass-loss rate. This degradation behavior is significantly different from that of pure bulk polyester implants [13].

2.5.2. Immuno-modulation effect of CFSCs

We further analyzed the detailed inflammatory responses using immunochemistry. M1 macrophages produce pro-inflammatory factors, whereas M2 macrophages secrete anti-inflammatory factors to promote tissue repair [51–54]. M2 and M1 are highlighted by their characteristic antibody markers CD206 and iNOS respectively (Fig. 6e). The CD206/iNOS ratio can reflect the M2/M1 polarization and thus indicate the outcome of tissue healing [55,56]. Once the inflammatory response is modulated toward favorable tissue repair, fibrosis is reduced, and simultaneously the process of vascularization is initiated.

At 30 days, M2 cells are highly expressed in all groups, whereas M1 cells are not significantly expressed. After 90 days, M2 macrophages gradually assume a predominant role in CFSCs groups, regulating the inflammatory response to facilitate tissue repair, whereas M1 cells dominate in the case of the PCL group. At 180 days, M2 expression in the PCL group decreases to its lowest level, while significantly overexpressed M2 and M1 populations surround the 20%-CFSCs and 40%-CFSCs. The sustained immune response lacking in pure PCL imparts to CFSCs tunable cell-mediated resorptive properties, consistent with the semi-quantitative *in vivo* biodegradation results from Masson images. Meanwhile, quantitative analysis of the fluorescence reveals that the M2/M1 ratio for 20%-CFSCs and 40%-CFSCs is as high as 3 and 4 (Fig. 6g), respectively. This signifies that these inflammations are strongly modulated by fiber silk to favor tissue repair and vascular regeneration for CFSCs.

To verify the modulative effect of CFSCs, we further conducted an *in vitro* macrophage cell RAW264.7 experiment (refer to methods section 4.11.3). The three groups of materials, PCL, 20%-CFSCs, and 40%-CFSCs were treated to simulate the long-term *in vivo* degradation impact using strong alkaline following a reported method [57]. The materials appeared surface-degraded to similar extents to the 180 days degradation *in vivo*. The macrophages differentiated toward M2 type for the 40%-CFSCs on Day 5 (Fig. S23). The ratio of CD206/CD86 corresponding to M2/M1 was significantly greater (Fig. S24).

2.5.3. Vascular regeneration potential

Vascular regeneration often occurs when M2 macrophages are recruited in a large number [58,59]. Platelet endothelial cell adhesion molecule (CD31) is a marker of vascular endothelial cells [60]. In Fig. 6f, after 30 days CD31 is not significantly expressed in any of the groups. At 90 days, 20%-CFSCs exhibits many tubular structures, whereas 40%-CFSCs shows a comparatively diminished CD31 level. This corresponds with the above M2 polarization results, indicating that 40%-CFSCs only began to activate M2 polarization of macrophages as it approached 90 days. Between 90 and 180 days, the platelet endothelial cells in 20%-CFSCs gradually increased along with the increased

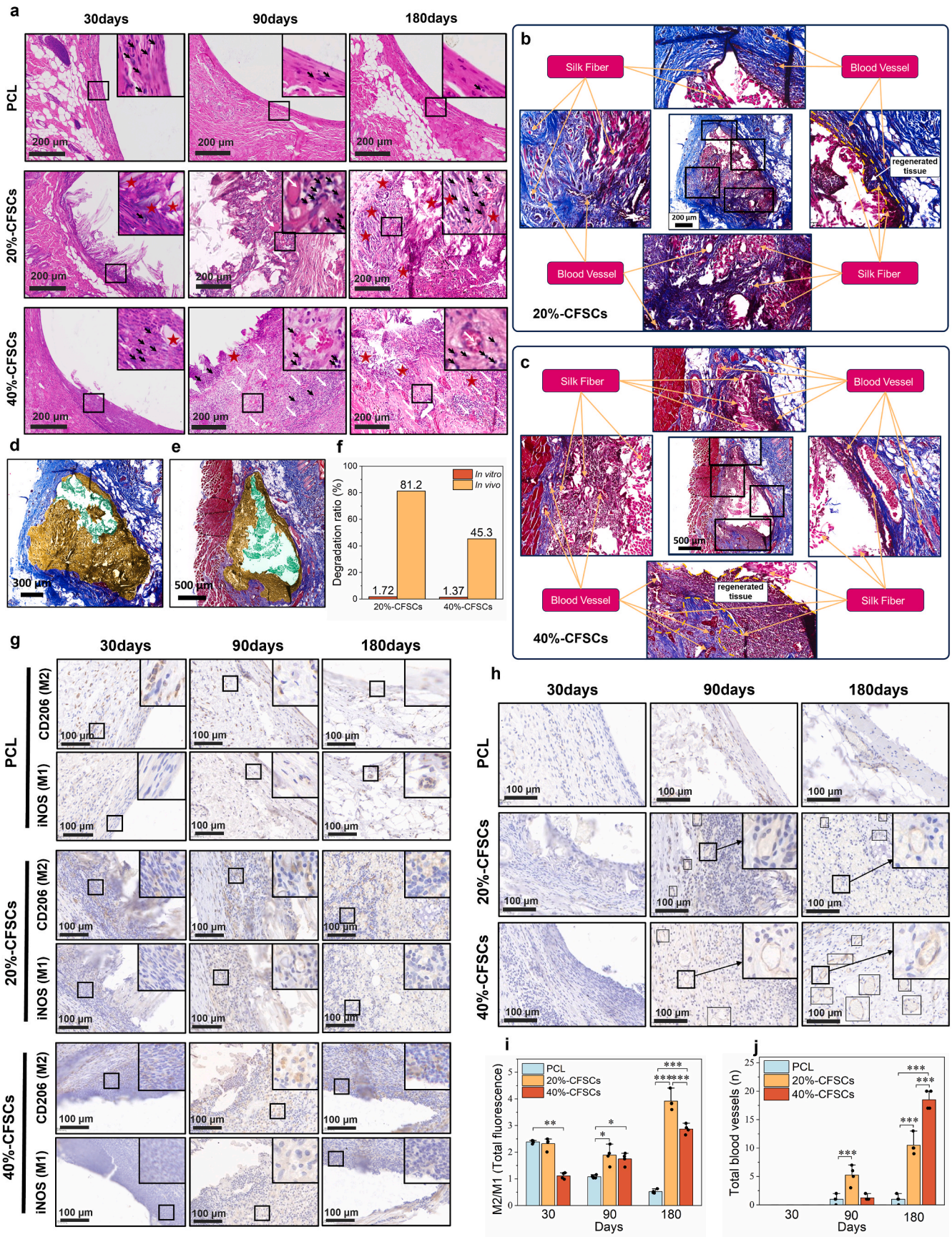

(caption on next page)

Fig. 6. *In vivo* compatibility assessment and immunohistochemistry analysis. (**a**) Hematoxylin-eosin (H&E) staining and analysis of the implant-tissue interface after 30 days, 90 days, and 180-days post-implantation in the subcutaneous rat model; fiber silk (red stars), inflammatory cells (black arrows), vascular structures (white arrows). (**b and c**) Artificially colored Masson's images of the 20%-CFSCs group (b) and 40%-CFSCs group (c) at 180-days of *in vivo* degradation (yellow represents newly formed tissue within the material, while green/white signifies remaining material). (**d**) *In vivo* degradation rate of 20%-CFSCs and 40%-CFSCs groups through semi-quantitative analysis, and *in vitro* degradation rate of 20%-CFSCs and 40%-CFSCs groups (n = 2). (**e, f**) Immunohistochemistry analysis for distribution of CD206-marked M2 and iNOS-marked M1 macrophages (e) and distribution of CD31-marked platelet endothelial cells that indicate vascular regeneration (f). Squared regions highlight individual blood vessels. (**g, h**) Quantifications of M2/M1 macrophage ratios (g) and total blood vessels indicating vascularization (h) (n = 4). One-way analysis of variance (ANOVA) was used to determine statistical differences between the groups (n = 4). The statistical significance was designated as * for $p < 0.05$, ** for $0.01 < p < 0.05$, and *** for $0.001 < p < 0.01$.

diameters of tubular structures. At 180 days, 40%-CFSCs demonstrated significantly elevated levels of CD31 expression, accompanied by the prevalent presence of tubular structures. In contrast, CD31 was not expressed in the PCL group. As shown in the Masson analysis (Figs. S19 and S20), abundant large-diameter blood vessels surround CFSCs, confirming a positive tissue repair process. Quantitative analysis also showed 40%-CFSCs regenerated the greatest number of blood vessels (Fig. 6h).

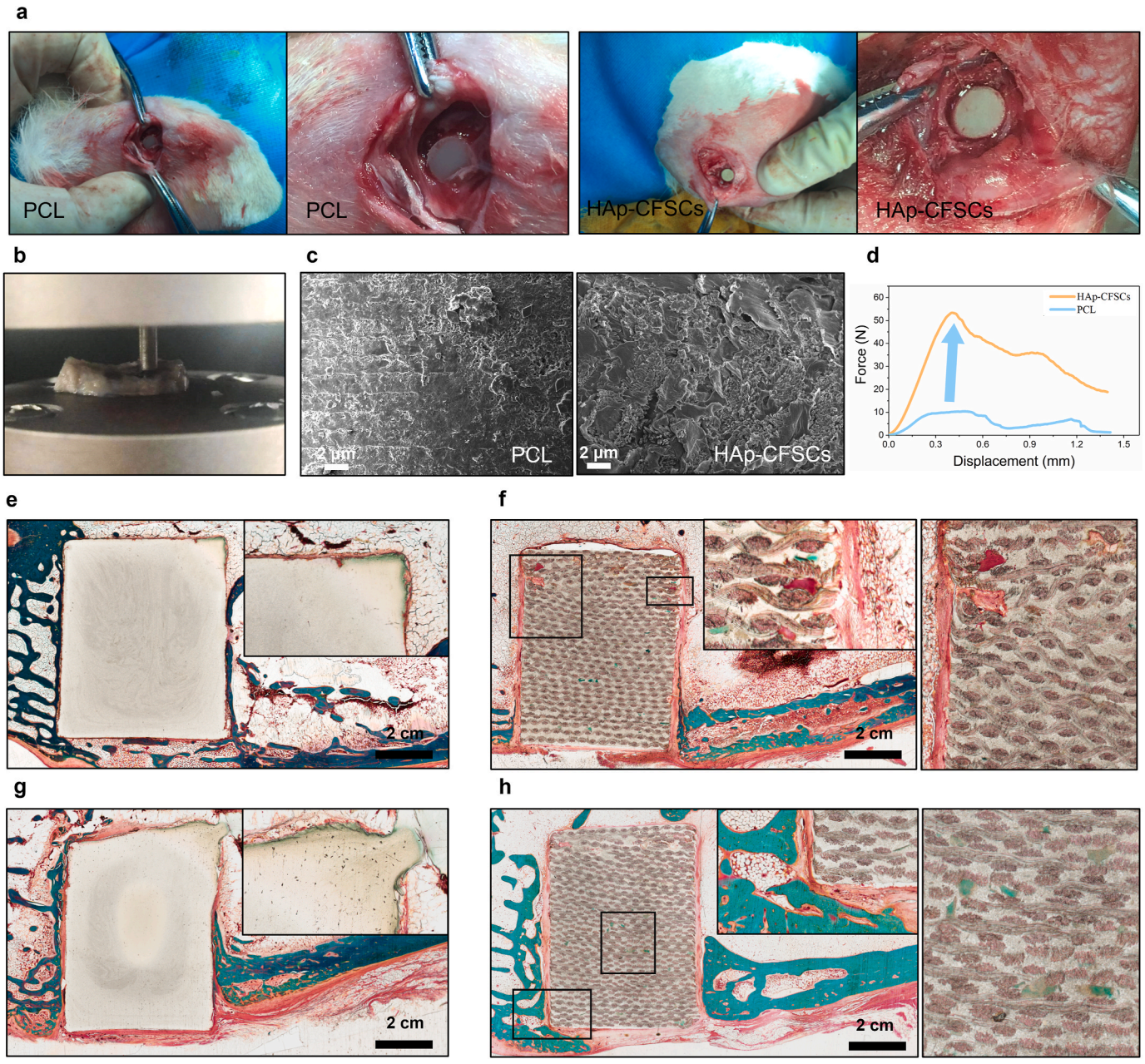

Fig. 7. HAp-CFSCs for artificial bones. (**a**) The surgical procedure of inserting PCL and HAp-CFSCs nail. (**b**) The push-out experiment. (**c**) Surface morphology from SEM of PCL and HAp-CFSC nail after 6 weeks. (**d**) The force-displacement curves of PCL and HAp-CFSC nail in push-out experiments (n = 2). (**e, g**) Goldner's trichrome analysis of the cylindrical bone defect model in the rabbit lateral femoral condyle using a PCL nail after 6 weeks (e) and 12 weeks (g). (**f, h**) Goldner's trichrome analysis of the cylindrical bone defect model in the rabbit lateral femoral condyle using a HAp-CFSC nail after 6 weeks (f) and 12 weeks (h).

2.5.4. Functional assessments in a rabbit tibial defect model

To further assess the biocompatibility with bone tissue and load-bearing capacity of CFSCs *in vivo*, we conducted an implantation experiment in a rabbit tibial defect model (Fig. 7a). Hydroxyapatite (HAp) as an osteogenic compound was incorporated into the PCL of CFSCs, with a pure PCL bulk material serving as the control group. Notably, the introduction of HAp was only for improved bone tissue conductance, and it didn't affect the mechanical properties of CFSCs (Fig. S25).

A push-out experiment was conducted to quantify the mechanical properties of implant and the implant-bone tissue integration (Fig. 7b). SEM imaging showed that HAp-CFSCs groups have a rougher surface (Fig. 7c). It revealed a significant improvement in the bonding strength for the HAp-CFSCs group compared to the PCL group (Fig. 7d). After 12 weeks, the PCL group exhibited obvious deformation due to insufficient mechanical properties (Fig. 7g). After 6 weeks, sporadic regions of new bone (stained in green) began to emerge for the CFSCs group (Fig. 7f). After 12 weeks, the surrounding bone tissue in the HAp-CFSCs group was abundant (Fig. 7h). No discernible signs of fracture in the composite were seen throughout the implantation period.

2.6. Comprehensive performance of CFSCs as a potential bone implant

We compared CFSCs with mainstream bone substitute materials for various critical properties (Fig. 8a). It demonstrated that although magnesium alloys are degradable, their initial modulus might be too high to match the modulus of majority bone tissues (*e.g.*, vertebral cancellous bone modulus is only 0.4 GPa). Degradable bulk polymers such as PLA and PCL lack sufficient strength and are pro-inflammatory. PEEK is non-degradable and exhibits low tissue integration. Bulk silk fibroin 'resin' is brittle and quickly loses most of its mechanical strength in aqueous environments.

The primary degradation mechanism of most mainstream degradable bone implants *in vivo* is bulk corrosion or hydrolysis. In contrast, the main *in vivo* degradation mechanism of CFSCs is surface-degradation actively mediated by the host cells (Fig. 8b). By adjusting the silk content, CFSCs can be adaptable to optimal degradation behavior and dynamically interact with cells and tissue for desirable repair and regeneration performance.

3. Conclusion

In this study, we selected continuous fiber silk and degradable polyester PCL to fabricate composites for implants for tissue regeneration. CFSCs successfully integrate key characteristics such as compatible modulus, high strength and toughness, long-term mechanical stability *in vitro*, hydrophilicity, and degradability *in vivo*. These properties could effectively avert issues like stress shielding, osteoporosis, mismatched degradation rates, mechanical failures, and secondary surgeries. To the best of our knowledge, CFSCs appear to be the closest to an ideal degradable bone implant to possess all these characteristics. We also revealed the facile processing performance and post-processing machinability of CFSCs. Although we identified that the primary *in vivo* degradation mechanism of CFSCs as cell-mediated absorption, our understanding on the underline molecular and cellular pathways is limited. We aspire to investigate on the active material-stimulated cell-mediated degradation behavior of CFSCs in future research. Taken together, our findings would inspire more work to expand the material family of fiber silk composites and bring forward more viable materials toward clinical implants.

4. Materials and methods

4.1. Materials

Degummed plain woven silk fabrics were purchased from the Beijing Rui Fu Xiang Silk Store (Beijing, China). The silk fabric's areal density was 0.95 kg m^{-2}. The estimated density of the fiber silk was 1300 kg m^{-3}. PCL (Mn = 80,000) and PLA (Mn = 80,000) were purchased from Macklin (Shanghai, China). Unless otherwise stated, the additional chemicals were acquired from Macklin (Shanghai China).

4.2. Fabrication of continuous fiber silk composites (CFSCs)

Degummed silk fabrics were firstly cleaned in deionized water under ultrasonication for 30 min, followed by a 2-h sterilization process within a high-temperature sterilization chamber. PLA and PCL particles were first hot-pressed at 500 kPa and 120 °C for 10 min and subsequently allowed to cool to room temperature, forming films. These films were then pressure-driven fusion together with a single layer of silk fabric at 500 kPa for 10 min to produce silk prepreg. Finally, different silk

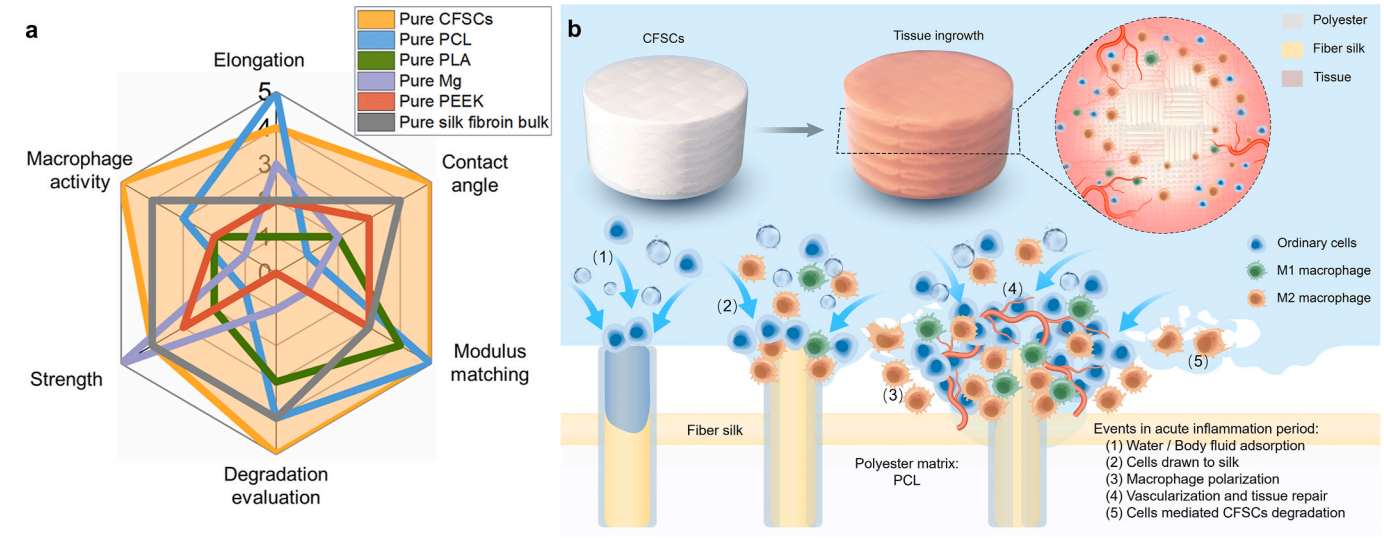

Fig. 8. (**a**) Comprehensive comparative analysis of key performance indications in a score radar chart for structural biomaterials, including CFSCs and other mainstream materials. (Some performance results have a difference of a hundredfold or are unquantifiable, so a scoring mechanism was used. Detailed data of the plotted indexations are shown in Table S1. (**b**) Illustrations of key events during the 180-days degradation *in vivo* of the CFSCs.

prepregs were assembled layer-by-layer in the mold as required; these were then pressure-driven fusion at 500 kPa for 20 min followed by natural cooling to ambient temperature. The thickness and quantity of silk prepreg layers required for CFSCs with different fiber volume fractions were calculated using the density method. All temperatures for pressure-driven fusion were 120 °C when PCL was used as the matrix polymer; however, it was 170 °C when PLA was used as the matrix polymer.

The hydroxyapatite (HAp) with a particle size of 80 nm and PCL were dissolved in acetic acid solution at a ratio of 1:10, and then stirred for 2 h. The mixture was then placed in ethanol at −20 °C, with the ethanol solution changed every day. After one week of replacement, the modified PCL was obtained. The CFSCs (fiber silk content is 40 %) prepared using this PCL were referred to as HAp-CFSCs.

4.3. Morphology analysis

Scanning electron microscopy (SEM, JEOL JSM-6010, Japan) was used to observe the microstructure during phosphate buffered saline solution (PBS) immersion experiments of the CFSCs. Specimens were sputter-coated with gold after being vacuum dried for 48 h.

A super depth-of-field microscopy (KEYENCE VHX-7000, Japan) was used to observe the surface morphology changes during PBS immersion experiments of the CFSCs. Specimens were vacuum dried for 48 h.

4.4. Tensile testing

Fiber silk were carefully taken out from the weft direction of the silk fabric and then glued to a tailor-made paper frame. As received and thermally treated fiber silk were tested, and the properties were analyzed following the procedures described in the Supplementary Materials.

Uniaxial tensile properties of the CFSCs were evaluated at a strain rate of 2 mm s^{-1} on the Instron 8801 screw-driven testing machine (Instron Corp, Norwood, MA, USA) following the standard testing method ISO 527-1 [61]. The tensile elastic modulus was estimated from the linear region of the stress-strain curve between 0.5 % and 3 % strain.

4.5. Compression testing

The compressive properties of the CFSCs were evaluated at a strain rate of 2 mm s^{-1} on an Instron 8801 screw-driven testing machine (Instron Corp, Norwood, MA, USA). The specimens were 12 mm long, 5 mm wide and 5 mm thick. A beam displacement rate was used with the compressive elastic modulus estimated from the linear region between 0.5 % and 3 % strain. For the degradation samples, wet compression tests were conducted on degraded samples within 5 min of leaving the PBS solution.

4.6. Interlaminar shear test

Interlaminar shear tests were conducted at a strain rate of 1 mm s^{-1} on an Instron 8801 screw-driven testing machine following the standard testing method ISO 14130 [62].

4.7. Surface wettability measurement

Static contact angle measurements of water on the surface of the specimens were performed on an OCA-20 (Dataphysics, Germany) at 25 °C. Average values from five measurements of one sample were determined.

4.8. Dynamic mechanical thermal analysis

A dynamic mechanical thermal analysis (DMA) was conducted on dry degradation samples using a DMA Q800 (TA Instrument, Waters Ltd.). The test samples had a length-to-thickness ratio of 5. The tests were run in a three-point bending mode at a frequency of 1 Hz and dynamic deformation strain of 0.1 %. The temperature was gradually increased from −80 °C to 40 °C at a rate of 3 °C per minute.

4.9. Raman spectroscopy and analysis of CFSCs

Changes in the interfacial regions during degradation of CFSCs were detected using the Raman imaging technique [63]. A Renishaw inVia Raman microscope (Renishaw, inVia, UK) was used, equipped with a 785 nm laser, an objective (Leica, 100 ×, NA = 0.85), and a 1200 l/mm grating. Raman spectroscopy measurements were performed on dry samples in StreamHR mode with a step size of 100 nm, an exposure time of 0.1 s, and 100 % laser power. The test measurement area varied in size but was arranged to cover the entire fiber interface area. Cosmic ray removal, noise filtering, and normalization methods were used to preprocess the acquired spectra [64]. Colored images were then obtained using a multivariate data analysis method involving the selection of the reference composition of *B. mori* silk [65], using the accessory software (Wire 4.3), and the recalculation of PCL distributions that surrounded the fibers.

4.10. In vitro degradation analysis

The specimens for *in vitro* degradation were of the same dimensions as those for the compression tests. A PBS buffer at 37 °C was used for the *in vitro* degradation experiment. Specimens were taken out at 3 days, 7 days, 14 days, 1 month, 2 months, 3 months, and 6 months. The specimens were washed with deionized water to remove residual PBS salt before mechanical and other measurements. At least 4 specimens were repeated for compression measurements.

To simulate the substantial degradation of the composites *in vivo*, we constructed an accelerated *in vitro* degradation model based on a reported method in Ref. [57]. The specimens were placed in a 4M sodium hydroxide solution at 37 °C for 48 h. Afterwards, the specimens were removed from the solution and immersed in deionized water for three days, with the water being replaced every 12 h. Finally, the specimens were taken out and allowed to air dry naturally.

4.11. In vitro cell experiments

4.11.1. Cell proliferation experiment

After UV sterilization, each group of materials was transferred to a 96 well plate, and 20 μl of high concentration MC3T3-E1 cell suspension (1×10^4 cells/well) was added to the surface of each material. After incubation for 2 h, the cells on the materials stabilized and adhered. A cell suspension (1×10^4 cells/100 μl) was then added to continue cultivation with the culture medium changed every other day. 10 μl of CCK8 reagent was added on days 1, 3, and 5 followed by incubation for 2 h to measure the optical density (OD) of 450 nm for each group using an enzyme-linked immunosorbent assay.

To test the effect of each group of materials on cell viability, the materials were first placed in a 24-well plate and co-cultured with MC3T3-E1 cell suspension at a density of 2×10^5 cells per well for 5 days. The materials were then taken out and 500 μL of live/dead cell assay kit combined dye (Beyotime, China) was added. After incubating at room temperature in the dark for 30 min, the supernatant was discarded and the plate was washed three times with PBS. Finally, the staining of dead (red)/live (green) cells was observed using a fluorescence microscope (IX71-22FL/P, Olympus, Japan).

4.11.2. Cell adhesion experiment

After UV sterilization, each group of materials was added to a 48 well plate, and 20 μl of high concentration MC3T3-E1 cell suspension (5×10^4 cells/well) was added to the surface of each material. This was allowed to incubate for 2 h to ensure stable adhesion on the material,

and then 500 μl of the complete medium was supplied for further incubation for 5 days. On the fifth day, the culture solution was aspirated, and 4 % paraformaldehyde was fixed on ice for 15 min, followed with 0.2 % Triton X-100 to permeate cells at room temperature for 5 min. Diluted fluorescent labeled Phalloidin (CoraLite ® 594 Phalloitin working solution) was added and incubated at room temperature in the dark for 20 min, prior to DAPI dye solution being added for 10 min at room temperature again in the dark. Laser confocal microscopy was used for observation and photography.

4.11.3. Macrophage cell experiment

In order to evaluate the *in vitro* immunomodulation properties of the composites, the *in vitro* accelerated material-degradation model was first constructed. Then, each group of degradation materials was placed in a six-well plate, and RAW 264.7 macrophage suspension (5×10^5 cells per well) was added to co-culture for 1 day. The cells were digested and fixed on ice with 4 % paraformaldehyde for 15 min. Then, the cell membrane was permeabilized for 15 min. Subsequently, the cells were incubated in the dark with M1 marker anti mouse PE conjugated CD86 (BioLegend, USA) and M2 marker APC conjugated CD206 (BioLegend, USA) for 15 min. After washing twice with PBS buffer, the cells were resuspended and the expression of specific M1 and M2 markers was detected on a flow cytometer (BD FACCanto II, USA). Finally, the data was processed using FlowJo software (TreeStar, Ashland, OR, USA). Calculate the ratio of CD206/CD86 corresponding to M2/M1 to confirm the immuno-modulative effects *in vivo*.

4.12. In vivo degradability assessments in a rat subcutaneous implantation model

To evaluate the histocompatibility of the material and observe the reaction of surrounding cells and tissues to the material, a total of 12 Sprague-Dawley (SD) rats (male, 10 weeks old) purchased from Yaokang Company (Approval number: SCXK2020-034) was used as a model for subcutaneous implantation. The CFSCs were cut into cubes with a side length of 2 mm. Silk fabric was cut into squares with a side length of 2 mm. PCL particles with a diameter of ~2 mm were used. All the implant materials were sterilized by Co60 radiation. 12 SD rats were randomly divided into three groups corresponding to three time points. For each rat, silk fabric, PCL, 20%-CFSCs and 40%-CFSCs, were implanted in the four dorsal sites; and for each time point, 4 rats were used for repeated tests. Then the rats were euthanized after 1, 3 and 6 months. The implant material specimens with adjacent tissue and major organs such as heart, liver and lung were collected for H&E staining and histological examination.

For immunohistochemistry analysis, the slide was dewaxed with xylene and graded with alcohol hydration, then treated with 3 % H_2O_2 for 15 min to block endogenous peroxidase activity. Antigen repair was performed in boiling sodium citrate buffer (pH 6.0) for 10 min before the slide was incubated with 10 % normal goat serum for 15 min followed by incubating overnight with CD206, iNOS and CD31 antibodies at 4 °C in a dark room. After washing three times with PBS, the slide was incubated with the second antibody at 37 °C for 30 min; the immune reactivity was observed by incubating with diaminobenzidine (DAB, Sigma Aldrich) and background counterstaining stained by Hematoxylin. To quantitatively analyze the material tissue staining intensity, four random shots per slide were taken and analyzed by Image Pro Plus 6.0 (IPP, Media Cybernetics, BD Biosciences) software; the images were finally converted into grayscale values for statistical comparison of each group.

4.13. In vivo functionality assessments in a rabbit distal femoral bone defect model

4.13.1. Implantation experiment for rabbit bone function restoration

A cylindrical bone defect repair model for rabbits lateral femoral condyle was established. New Zealand rabbits (of weight ~3 kg) were randomly divided into HAp-CFSCs composites and pure PCL bulk groups (each group with three rabbits). All animal operations and experiments were approved by SYDW 2022039. The rabbits were anesthetized with a solution (3 %) of phenobarbital sodium at a dose of 0.5 mL/kg under sterile conditions. The knee joint was fixed at maximum extension with the hind limb was shaved. A 2 cm longitudinal incision was made lateral to the patellar ligament to expose the lateral femoral condyle. A cylindrical bone defect 5 mm in diameter and 8 mm in depth was formed via drilling followed by implantation of the two group materials (PCL and HAp-CFSCs). After six weeks, all rabbits (with six left and six right femur specimens from each group) were sacrificed. The left femurs (three specimens in each group) were then cut into undecalcified histological slices for Goldner's trichrome staining, and the right femurs (three specimens in each group) were prepared for mechanical push-out testing.

4.13.2. Histopathological analysis

Three left femur specimens in each group were fixed in formalin, dehydrated with ethanol, and then embedded in polymethylmethacrylate (three left rabbits per group). The embedded specimens were cut, ground, and polished. The ground sections of 40–50 μm were then subjected to Goldner's trichrome staining (bone tissues were stained green, osteoid tissues were stained orange red) to assess soft-tissue in-growth and bone formation. The entire stained sections were photographed by a microscope (Zeiss AX10 imager M2, Germany).

4.13.3. Push-out testing of bone implant

A mechanical testing system (Instron Corp, Norwood, MA, USA) was applied to evaluate the integrated strength between the implant and the bone at six weeks. Briefly, three right femur specimens in each group were carefully cut to expose the two side of the implant before testing. A custom-designed special vertically matched hollow base (7 mm in diameter) and a cylindrical pressing shaft were applied to ensure loading alignment. The push-out testing was then carried out at a constant speed of 1 mm/min until the implant and bone interface were separated by the presence of an abrupt drop, prior to the loading curve being recorded to compare the bonding strength between implanted materials and tissues.

4.14. Statistical analysis

Mechanical testing, static contact angle testing, was repeated on $5 \geq n \geq 3$ specimens of the same sample. Data are expressed as mean ± standard deviation (mean ± SD). Statistical analysis was carried out using SPSS 16.0 software, and one-way ANOVA with Tukey's post hoc test was performed to determine the significant differences between groups. The statistical significance was designated as * for $p < 0.05$, ** for $0.01 < p < 0.05$, and *** for $0.001 < p < 0.01$.

CRediT authorship contribution statement

Wenhan Tian: Writing – original draft, Methodology, Investigation, Formal analysis. **Yuzeng Liu:** Writing – review & editing, Supervision, Resources, Funding acquisition, Conceptualization. **Bo Han:** Writing – review & editing, Investigation, Formal analysis. **Fengqi Cheng:** Writing – review & editing, Investigation, Formal analysis. **Kang Yang:** Writing – review & editing, Investigation, Formal analysis. **Weiyuan Hu:** Investigation, Formal analysis. **Dongdong Ye:** Writing – review & editing, Methodology, Formal analysis. **Sujun Wu:** Writing – review & editing, Supervision, Resources. **Jiping Yang:** Writing – review & editing, Supervision, Resources, Conceptualization. **Qi Chen:** Writing – review & editing, Resources. **Yong Hai:** Writing – review & editing, Resources, Conceptualization. **Robert O. Ritchie:** Writing – review & editing, Resources, Conceptualization. **Guanping He:** Writing – review & editing, Methodology, Investigation, Formal analysis. **Juan Guan:**

Writing – review & editing, Supervision, Resources, Funding acquisition, Conceptualization.

Ethics approval and consent to participate

All animal operations and experiments were approved by SYDW 2022039.

Declaration of competing interest

The authors declare the following personal relationships which may be considered as potential competing interests: Qi Chen is currently employed by Ningbo Regen Biotech Co., Ltd.

Acknowledgements

We acknowledge Mr. Xiaoyang Fan for the help with ultra-depth optical scope and atomic force microscope measurements. The funding from the following funders is acknowledged: National Natural Science Foundation of China (No. 82203893 and No. 52473090); Capital Medical University (Clinical and Basic Research on Lumbar Multiple Trajectory Screw Internal Fixation Technology, CYFH202316); the Anhui Provincial Excellent Youth Fund Project (2408085Y025).

Appendix A. Supplementary data

Supplementary data to this article can be found online at https://doi.org/10.1016/j.bioactmat.2024.11.036.

References

[1] G.L. Koons, M. Diba, A.G. Mikos, Materials design for bone-tissue engineering, Nat. Rev. Mater. 5 (2020) 584–603, https://doi.org/10.1038/s41578-020-0204-2.
[2] A.-M. Pobloth, S. Checa, H. Razi, A. Petersen, J.C. Weaver, K. Schmidt-Bleek, M. Windolf, A.Á. Tatai, C.P. Roth, K.-D. Schaser, G.N. Duda, P. Schwabe, Mechanobiologically optimized 3D titanium-mesh scaffolds enhance bone regeneration in critical segmental defects in sheep, Sci. Transl. Med. 10 (2018), https://doi.org/10.1126/scitranslmed.aam8828 eaam8828.
[3] M. Bohner, L. Galea, N. Doebelin, Calcium phosphate bone graft substitutes: failures and hopes, J. Eur. Ceram. 32 (2012) 2663–2671, https://doi.org/10.1016/j.jeurceramsoc.2012.02.028.
[4] F. Barthelat, Growing a synthetic mollusk shell, Science 354 (2016) 32–33, https://doi.org/10.1126/science.aah6507.
[5] M. Alizadeh-Osgouei, Y. Li, C. Wen, A comprehensive review of biodegradable synthetic polymer-ceramic composites and their manufacture for biomedical applications, Bioact. Mater. 4 (2019) 22–36, https://doi.org/10.1016/j.bioactmat.2018.11.003.
[6] C.J. Hernandez, G.S. Beaupré, T.S. Keller, D.R. Carter, The influence of bone volume fraction and ash fraction on bone strength and modulus, Bone 29 (2001) 74–78, https://doi.org/10.1016/s8756-3282(01)00467-7.
[7] E.F. Morgan, G.L. Barnes, T.A. Einhorn, The bone organ system: form and function, in: Osteoporosis, Elsevier, 2008, pp. 3–25, https://doi.org/10.1016/b978-012370544-0.50003-3.
[8] A.K. Nair, A. Gautieri, S.-W. Chang, M.J. Buehler, Molecular mechanics of mineralized collagen fibrils in bone, Nat. Commun. 4 (2013) 1724, https://doi.org/10.1038/ncomms2720.
[9] Z.U. Arif, M.Y. Khalid, R. Noroozi, A. Sadeghianmaryan, M. Jalalvand, M. Hossain, Recent advances in 3D-printed polylactide and polycaprolactone-based biomaterials for tissue engineering applications, Int. J. Biological Macromol. 218 (2022) 930–968, https://doi.org/10.1016/j.ijbiomac.2022.07.140.
[10] D.S. Sparks, F.M. Savi, C.E. Dlaska, S. Saifzadeh, G. Brierly, E. Ren, A. Cipitria, J. C. Reichert, M.-L. Wille, M.A. Schuetz, N. Ward, M. Wagels, D.W. Hutmacher, Convergence of scaffold-guided bone regeneration principles and microvascular tissue transfer surgery, Sci. Adv. 9 (2023), https://doi.org/10.1126/sciadv.add6071.
[11] D. Zhao, T. Zhu, J. Li, L. Cui, Z. Zhang, X. Zhuang, J. Ding, Poly(lactic-co-glycolic acid)-based composite bone-substitute materials, Bioact. Mater. 6 (2021) 346–360, https://doi.org/10.1016/j.bioactmat.2020.08.016.
[12] L. Li, Q. Li, L. Gui, Y. Deng, L. Wang, J. Jiao, Y. Hu, X. Lan, J. Hou, Y. Li, D. Lu, Sequential gastrodin release PU/n-HA composite scaffolds reprogram macrophages for improved osteogenesis and angiogenesis, Bioact. Mater. 19 (2023) 24–37, https://doi.org/10.1016/j.bioactmat.2022.03.037.
[13] M. Bartnikowski, T.R. Dargaville, S. Ivanovski, D.W. Hutmacher, Degradation mechanisms of polycaprolactone in the context of chemistry, geometry and environment, Prog. Polym. Sci. 96 (2019) 1–20, https://doi.org/10.1016/j.progpolymsci.2019.05.004.
[14] M. Suchenski, M.B. McCarthy, D. Chowaniec, D. Hansen, W. McKinnon, J. Apostolakos, R. Arciero, A.D. Mazzocca, Material properties and composition of soft-tissue fixation, Arthroscopy 26 (2010) 821–831, https://doi.org/10.1016/j.arthro.2009.12.026.
[15] F.M. Najafabadi, S. Karbasi, S.Z. Benisi, S. Shojaei, Physical, mechanical, and biological performance of chitosan-based nanocomposite coating deposited on the polycaprolactone-based 3D printed scaffold: potential application in bone tissue engineering, Int. J. Biol. Macromol. 243 (2023) 125218, https://doi.org/10.1016/j.ijbiomac.2023.125218.
[16] J. Liu, B. Liu, S. Min, B. Yin, B. Peng, Z. Yu, C. Wang, X. Ma, P. Wen, Y. Tian, Y. Zheng, Biodegradable magnesium alloy WE43 porous scaffolds fabricated by laser powder bed fusion for orthopedic applications: process optimization, in vitro and in vivo investigation, Bioact. Mater. 16 (2022) 301–319, https://doi.org/10.1016/j.bioactmat.2022.02.020.
[17] M.A. Woodruff, D.W. Hutmacher, The return of a forgotten polymer—polycaprolactone in the 21st century, Prog. Polym. Sci. 35 (2010) 1217–1256, https://doi.org/10.1016/j.progpolymsci.2010.04.002.
[18] S. Balali, S.M. Davachi, R. Sahraeian, B. Shiroud Heidari, J. Seyfi, I. Hejazi, Preparation and characterization of composite blends based on polylactic acid/polycaprolactone and silk, Biomacromolecules 19 (2018) 4358–4369, https://doi.org/10.1021/acs.biomac.8b01254.
[19] K.L. Wong, C.T. Wong, W.C. Liu, H.B. Pan, M.K. Fong, W.M. Lam, W.L. Cheung, W. M. Tang, K.Y. Chiu, K.D.K. Luk, W.W. Lu, Mechanical properties and in vitro response of strontium-containing hydroxyapatite/polyetheretherketone composites, Biomaterials 30 (2009) 3810–3817, https://doi.org/10.1016/j.biomaterials.2009.04.016.
[20] D. da Silva, M. Kaduri, M. Poley, O. Adir, N. Krinsky, J. Shainsky-Roitman, A. Schroeder, Biocompatibility, biodegradation and excretion of polylactic acid (PLA) in medical implants and theranostic systems, Chem. Eng. J. 340 (2018) 9–14, https://doi.org/10.1016/j.cej.2018.01.010.
[21] M. Esmaily, J.E. Svensson, S. Fajardo, N. Birbilis, G.S. Frankel, S. Virtanen, R. Arrabal, S. Thomas, L.G. Johansson, Fundamentals and advances in magnesium alloy corrosion, Prog. Mater. Sci. 89 (2017) 92–193, https://doi.org/10.1016/j.pmatsci.2017.04.011.
[22] H. Yang, B. Jia, Z. Zhang, X. Qu, G. Li, W. Lin, D. Zhu, K. Dai, Y. Zheng, Alloying design of biodegradable zinc as promising bone implants for load-bearing applications, Nat. Commun. 11 (2020) 401, https://doi.org/10.1038/s41467-019-14153-7.
[23] F.G. Omenetto, D.L. Kaplan, New opportunities for an ancient material, Science 329 (2010) 528–531, https://doi.org/10.1126/science.1188936.
[24] J.D. van Beek, L. Beaulieu, H. Schäfer, M. Demura, T. Asakura, B.H. Meier, Solid-state NMR determination of the secondary structure of Samia cynthia ricini silk, Nature 405 (2000) 1077–1079, https://doi.org/10.1038/35016625.
[25] Z. Shao, F. Vollrath, Surprising strength of silkworm silk, Nature 418 (2002), https://doi.org/10.1038/418741a, 741–741.
[26] J. Pérez-Rigueiro, M. Elices, J. Llorca, C. Viney, Tensile properties of silkworm silk obtained by forced silking, J. Appl. Polym. Sci. 82 (2001) 1928–1935, https://doi.org/10.1002/app.2038.
[27] A. Nova, S. Keten, N.M. Pugno, A. Redaelli, M.J. Buehler, Molecular and nanostructural mechanisms of deformation, strength and toughness of spider silk fibrils, Nano Lett. 10 (2010) 2626–2634, https://doi.org/10.1021/nl101341w.
[28] M. Andersson, J. Johansson, A. Rising, Silk spinning in silkworms and spiders, IJMS 17 (2016) 1290, https://doi.org/10.3390/ijms17081290.
[29] J.L. Yarger, B.R. Cherry, A. van der Vaart, Uncovering the structure–function relationship in spider silk, Nat. Rev. Mater. 3 (2018) 18008, https://doi.org/10.1038/natrevmats.2018.8.
[30] C. Vepari, D.L. Kaplan, Silk as a biomaterial, Prog. Polym. Sci. 32 (2007) 991–1007, https://doi.org/10.1016/j.progpolymsci.2007.05.013.
[31] F. Vollrath, D. Porter, Spider silk as archetypal protein elastomer, Soft Matter 2 (2006) 377, https://doi.org/10.1039/b600098n.
[32] W. Huang, S. Ling, C. Li, F.G. Omenetto, D.L. Kaplan, Silkworm silk-based materials and devices generated using bio-nanotechnology, Chem. Soc. Rev. 47 (2018) 6486–6504, https://doi.org/10.1039/c8cs00187a.
[33] J. Hu, H. Albadawi, Z. Zhang, M.A. Salomao, S. Gunduz, S. Rehman, L. D'Amone, J. L. Mayer, F. Omenetto, R. Oklu, Silk embolic material for catheter-directed endovascular drug delivery, Adv. Mater. 34 (2021), https://doi.org/10.1002/adma.202106865.
[34] D. López Barreiro, Z. Martín-Moldes, J. Yeo, S. Shen, M.J. Hawker, F.J. Martin-Martinez, D.L. Kaplan, M.J. Buehler, Conductive silk-based composites using biobased carbon materials, Adv. Mater. 31 (2019) 1904720, https://doi.org/10.1002/adma.201904720.
[35] D.N. Rockwood, R.C. Preda, T. Yücel, X. Wang, M.L. Lovett, D.L. Kaplan, Materials fabrication from Bombyx mori silk fibroin, Nat. Protoc. 6 (2011) 1612–1631, https://doi.org/10.1038/nprot.2011.379.
[36] K.A. Burke, D.C. Roberts, D.L. Kaplan, Silk fibroin aqueous-based adhesives inspired by mussel adhesive proteins, Biomacromolecules 17 (2015) 237–245, https://doi.org/10.1021/acs.biomac.5b01330.
[37] C. Guo, C. Li, H.V. Vu, P. Hanna, A. Lechtig, Y. Qiu, X. Mu, S. Ling, A. Nazarian, S. J. Lin, D.L. Kaplan, Thermoplastic moulding of regenerated silk, Nat. Mater. 19 (2019) 102–108, https://doi.org/10.1038/s41563-019-0560-8.
[38] G. Cheng, X. Wang, S. Tao, J. Xia, S. Xu, Differences in regenerated silk fibroin prepared with different solvent systems: from structures to conformational changes, J. Appl. Polym. Sci. 132 (2015), https://doi.org/10.1002/app.41959.
[39] C. Li, C. Guo, V. Fitzpatrick, A. Ibrahim, M.J. Zwierstra, P. Hanna, A. Lechtig, A. Nazarian, S.J. Lin, D.L. Kaplan, Design of biodegradable, implantable devices

towards clinical translation, Nat. Rev. Mater. 5 (2019) 61–81, https://doi.org/10.1038/s41578-019-0150-z.
[40] J. Guan, D. Porter, F. Vollrath, Thermally induced changes in dynamic mechanical properties of native silks, Biomacromolecules 14 (2013) 930–937, https://doi.org/10.1021/bm400012k.
[41] C. Fu, D. Porter, Z. Shao, Moisture effects on *Antheraea pernyi* silk's mechanical property, Macromolecules 42 (2009) 7877–7880, https://doi.org/10.1021/ma901321k.
[42] F. Mesquita, C. Breite, S.V. Lomov, Y. Swolfs, In-situ synchrotron computed tomography tensile testing of composite specimens to estimate fibre strength Weibull parameters, Compos. Sci. Technol. (2022) 109710, https://doi.org/10.1016/j.compscitech.2022.109710.
[43] N. Graupner, S. Basel, J. Müssig, Size effects of viscose fibres and their unidirectional epoxy composites: application of least squares Weibull statistics, Cellulose 25 (2018) 3407–3421, https://doi.org/10.1007/s10570-018-1819-y.
[44] Y. Swolfs, I. Verpoest, L. Gorbatikh, Issues in strength models for unidirectional fibre-reinforced composites related to Weibull distributions, fibre packings and boundary effects, Compos. Sci. Technol. 114 (2015) 42–49, https://doi.org/10.1016/j.compscitech.2015.04.002.
[45] E. Trujillo, M. Moesen, L. Osorio, A.W. Van Vuure, J. Ivens, I. Verpoest, Bamboo fibres for reinforcement in composite materials: strength Weibull analysis, Compos. Part Appl. Sci. Manuf. 61 (2014) 115–125, https://doi.org/10.1016/j.compositesa.2014.02.003.
[46] R. Shi, D. Ye, K. Ma, W. Tian, Y. Zhao, H. Guo, Z. Shao, J. Guan, R.O. Ritchie, Understanding the interfacial adhesion between natural silk and polycaprolactone for fabrication of continuous silk biocomposites, ACS Appl. Mater. Interfaces 14 (2022) 46932–46944, https://doi.org/10.1021/acsami.2c11045.
[47] J. Thomason, G. Xypolias, Hydrothermal ageing of glass fibre reinforced vinyl ester composites: a review, Polymers 15 (2023) 835, https://doi.org/10.3390/polym15040835.
[48] H. Yu, J. Zhang, M. Fang, T. Ma, B. Wang, Z. Zhang, Z. Hu, H. Li, X. Cao, C. Ding, H. Deng, K. Yang, Bio-inspired strip-shaped composite composed of glass fabric and waste selvedge from A. pernyi silk for lightweight and high-impact applications, Compos. Part Appl. Sci. Manuf. 174 (2023) 107715, https://doi.org/10.1016/j.compositesa.2023.107715.
[49] K. Yang, H. Yu, X. Cao, J. Guan, S. Cai, Z. Yang, W. Huang, B. Wang, N. Qin, Z. Wu, W. Tian, S. Zhang, R.O. Ritchie, The critical role of corrugated lamellae morphology on the tough mechanical performance of natural Syncerus caffer horn sheath, Cell. Rep. Phys. Sci. 4 (2023) 101576, https://doi.org/10.1016/j.xcrp.2023.101576.
[50] Y. Wang, H. Zhang, Y. Hu, Y. Jing, Z. Geng, J. Su, Bone repair biomaterials: a perspective from immunomodulation, Adv. Funct. Mater. 32 (2022) 2208639, https://doi.org/10.1002/adfm.202208639.
[51] L. Xiao, H. Liu, H. Huang, S. Wu, L. Xue, Z. Geng, L. Cai, F. Yan, 3D nanofiber scaffolds from 2D electrospun membranes boost cell penetration and positive host response for regenerative medicine, J. Nanobiotechnol. 22 (2024) 322, https://doi.org/10.1186/s12951-024-02578-2.
[52] M. Locati, G. Curtale, A. Mantovani, Diversity, mechanisms, and significance of macrophage plasticity, Annu. Rev. Pathol. 15 (2020) 123–147, https://doi.org/10.1146/annurev-pathmechdis-012418-012718.
[53] J. Pajarinen, T. Lin, E. Gibon, Y. Kohno, M. Maruyama, K. Nathan, L. Lu, Z. Yao, S. B. Goodman, Mesenchymal stem cell-macrophage crosstalk and bone healing, Biomaterials 196 (2019) 80–89, https://doi.org/10.1016/j.biomaterials.2017.12.025.
[54] T.A. Wynn, A. Chawla, J.W. Pollard, Macrophage biology in development, homeostasis and disease, Nature 496 (2013) 445–455, https://doi.org/10.1038/nature12034.
[55] K. Dai, Z. Geng, W. Zhang, X. Wei, J. Wang, G. Nie, C. Liu, Biomaterial design for regenerating aged bone: materiobiological advances and paradigmatic shifts, Natl. Sci. Rev. 11 (2024) 76, https://doi.org/10.1093/nsr/nwae076.
[56] Z. Sun, R. Huang, H. Lyu, X. Yu, W. Wang, J. Li, X. Lu, C. Guo, Silk acid as an implantable biomaterial for tissue regeneration, Adv. Healthcare Mater. 12 (2023) 2301439, https://doi.org/10.1002/adhm.202301439.
[57] H. Wu, X. Wei, Y. Liu, H. Dong, Z. Tang, N. Wang, S. Bao, Z. Wu, L. Shi, X. Zheng, X. Li, Z. Guo, Dynamic degradation patterns of porous polycaprolactone/β-tricalcium phosphate composites orchestrate macrophage responses and immunoregulatory bone regeneration, Bioact. Mater. 21 (2022) 595–611, https://doi.org/10.1016/j.bioactmat.2022.07.032.
[58] S.-Y. Yang, Y.-N. Zhou, X.-G. Yu, Z.-Y. Fu, C.-C. Zhao, Y. Hu, K.-L. Lin, Y.-J. Xu, A xonotlite nanofiber bioactive 3D-printed hydrogel scaffold based on osteo-/angiogenesis and osteoimmune microenvironment remodeling accelerates vascularized bone regeneration, J. Nanobiotechnol. 22 (2024) 59, https://doi.org/10.1186/s12951-024-02323-9.
[59] J. Zhang, J. Muri, G. Fitzgerald, T. Gorski, R. Gianni-Barrera, E. Masschelein, G. D'Hulst, P. Gilardoni, G. Turiel, Z. Fan, T. Wang, M. Planque, P. Carmeliet, L. Pellerin, C. Wolfrum, S.-M. Fendt, A. Banfi, C. Stockmann, I. Soro-Arnáiz, M. Kopf, K. De Bock, Endothelial lactate controls muscle regeneration from ischemia by inducing M2-like macrophage polarization, Cell Metabol. 31 (2020) 1136–1153.e7, https://doi.org/10.1016/j.cmet.2020.05.004.
[60] R. Xu, A. Yallowitz, A. Qin, Z. Wu, D.Y. Shin, J.-M. Kim, S. Debnath, G. Ji, M. P. Bostrom, X. Yang, C. Zhang, H. Dong, P. Kermani, S. Lalani, N. Li, Y. Liu, M. G. Poulos, A. Wach, Y. Zhang, K. Inoue, A. Di Lorenzo, B. Zhao, J.M. Butler, J.-H. Shim, L.H. Glimcher, M.B. Greenblatt, Targeting skeletal endothelium to ameliorate bone loss, Nat. Med. 24 (2018) 823–833, https://doi.org/10.1038/s41591-018-0020-z.
[61] K. Monkova, P.P. Monka, R. Hricová, B. Hausnerova, L. Knapčíková, Tensile properties of four types of ABS lattice structures—a comparative study, Polymers 15 (2023) 4090, https://doi.org/10.3390/polym15204090.
[62] K.A. Weidenmann, L. Baumgärtner, B. Haspel, The edge shear test - an alternative testing method for the determination of the interlaminar shear strength in composite materials, MSF 825–826 (2015) 806–813. https://doi.org/10.4028/www.scientific.net/msf.825-826.806.
[63] Z. Yuan, D. Meng, Y. Wu, G. Tang, P. Liang, J.H. Xin, D. Ye, Raman imaging-assisted customizable assembly of MOFs on cellulose aerogel, Nano Res. 15 (2021) 2599–2607, https://doi.org/10.1007/s12274-021-3821-1.
[64] Q. Li, Z. Yuan, C. Zhang, S. Hu, Z. Chen, Y. Wu, P. Chen, H. Qi, D. Ye, Tough, highly oriented, super thermal insulating regenerated all-cellulose sponge-aerogel fibers integrating a graded aligned nanostructure, Nano Lett. 22 (2022) 3516–3524, https://doi.org/10.1021/acs.nanolett.1c03943.
[65] G. Fang, S. Sapru, S. Behera, J. Yao, Z. Shao, S.C. Kundu, X. Chen, Exploration of the tight structural–mechanical relationship in mulberry and non-mulberry silkworm silks, J. Mater. Chem. B 4 (2016) 4337–4347, https://doi.org/10.1039/c6tb01049k.